Interplay between charge density wave order and magnetic field in the nonmagnetic rare-earth tritelluride $LaTe_3$

Arnab Pariari,[1,2] Sudipta Koley,[3] Shubhankar Roy,[1,2] Ratnadwip Singha,[1,2,4]
Mukul S. Laad,[2,5] A. Taraphder,[6,7] and Prabhat Mandal[1,2]
[1]*Saha Institute of Nuclear Physics, 1/AF Bidhannagar, Kolkata 700 064, India*
[2]*Homi Bhabha National Institute, Trombay, Mumbai 400085, India*
[3]*Department of Physics, Amity Institute of Applied Sciences, Amity University, Kolkata 700135, India*
[4]*Department of Chemistry, Princeton University, Princeton, New Jersey 08540, USA*
[5]*Institute of Mathematical Sciences, Taramani, Chennai 600113, India*
[6]*Department of Physics and Centre for Theoretical Studies, Indian Institute of Technology, Kharagpur 721302, India*
[7]*School of Basic Sciences, Indian Institute of Technology, Mandi 751005, India*

(Received 22 May 2020; accepted 12 October 2021; published 25 October 2021)

Charge density wave (CDW) states in solids bear an intimate connection to underlying fermiology. Thus, modification of the latter by suitable perturbations provides an attractive handle to unearth CDW states. Here, we combine extensive magnetotransport experiments and first-principles correlated electronic structure calculations on nonmagnetic tritelluride $LaTe_3$ to uncover phenomena rare in CDW systems: (i) a humplike feature in temperature dependence of resistivity at low temperatures under application of magnetic-field (B), which moves to higher temperatures with increasing B, (ii) highly anisotropic large transverse magnetoresistance (MR) upon rotation of B about the current parallel to the crystallographic c axis, (iii) anomalously large positive MR with spikelike peaks at characteristic angles when the angle between current and field is varied on the bc plane, (iv) extreme sensitivity of the angular variation of MR on field and temperature. These observations find a comprehensive explication in theoretical picture that captures field-induced electronic structure modification in $LaTe_3$.

DOI: 10.1103/PhysRevB.104.155147

I. INTRODUCTION

Formation of charge density wave (CDW) order in solids spontaneously breaks the discrete translational symmetry of the lattice. As a direct consequence, the "normal-state" Fermi surface (FS) is destabilized due to CDW gap opening: In the simplest picture, the Fermi surface is completely obliterated by the opening of a full gap, whereas a partial gapping of the FS in a multiband system suppresses charge scattering, leading to enhanced Landau-quasiparticle-like coherence in the CDW state (notable examples are transition-metal dichalcogenides [1]). This implies lower resistivity and high carrier mobility. Quasi-two-dimensional rare-earth (R) tritellurides RTe_3, where R = Y, La-Sm, and Gd-Tm, have attracted significant interest due to the existence of CDW order [2–18] in a metal without the complications arising from a proximity to correlation-driven Mott transition and strong attendant magnetic fluctuations. These materials crystallize into a weakly orthorhombic (pseudotetragonal) structure consisting of double layers of square-planar Te sheets separated by corrugated RTe slabs [3,12–14,16]. The long b axis is perpendicular to the Te planes. In addition, the two neighboring Te square-net sheets exhibit van der Waals (vdW) gap between them, which allows exfoliation of bulk crystals into thin flakes. It has been established that this family of materials is a fertile ground for intriguing physics by tuning the CDW state through perturbations, such as chemical or external pressure [10,11,14,16,17]. Ru and co-workers reported a systematic variation of CDW transition temperature in RTe_3 (where R = Sm, Gd, Tb, Dy, Ho, Er, and Tm) with an increasing lattice parameter [10,11]. A systematic study of CDW stability as a function of the lattice parameter was also reported [4,19]. The CDW state in these materials rapidly suppresses, and superconductivity appears with the increase in applied pressure [14,17]. Also, a second CDW transition appears at a much lower temperature for the heavier members of the series, R = Dy, Ho, Er, and Tm [10,11,16,17]. However, no such phenomenon has been reported for $LaTe_3$ and other nonmagnetic members. $LaTe_3$ is the lightest member of this family of compounds where the CDW transition temperature (T_{CDW}) is presumed to be higher than 400 K [13]. $LaTe_3$ has been characterized by transmission electron microscopy [4], nuclear magnetic resonance [9], angle-resolved photoemission spectroscopy (ARPES) [12], band-structure calculation, de Haas–van Alphen oscillations [13], preliminary electronic transport [8,18], and thermodynamic property measurements [8]. Hitherto, these studies have sought mainly to understand the CDW-induced lattice modulation and accompanying Fermi-surface reconstruction.

In the absence of CDW order, the unmodulated Fermi surface comprises bands formed from the p_x and p_z orbitals of Te atoms in the square-planar layers: two diamond-shaped sheets made up of warped inner and outer layers on the ac

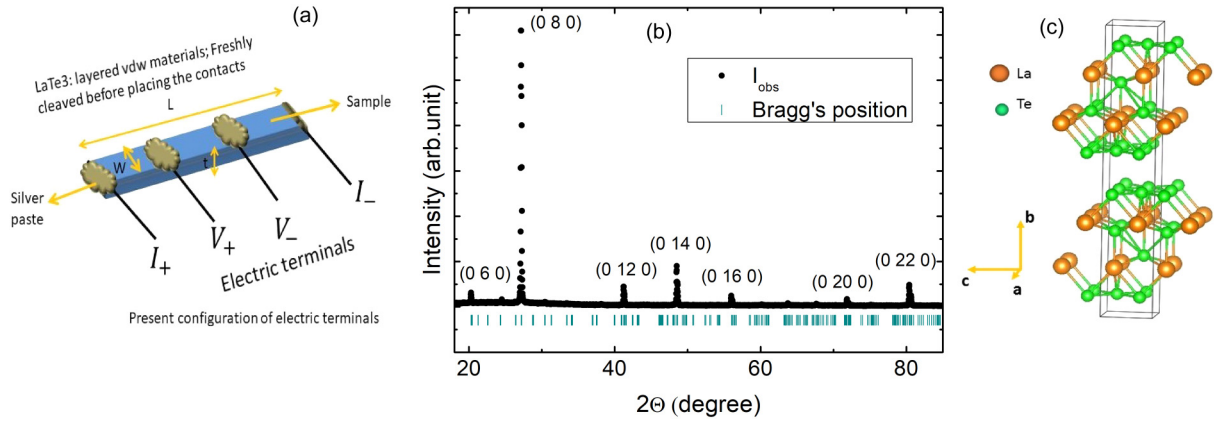

FIG. 1. Configuration of electrical contacts, x-ray diffraction on the single-crystal sample, and crystal structure of $LaTe_3$. (a) Four-probe electrical contacts on freshly cleaved single-crystal sample. (b) X-ray diffraction from the largest flat surface of the crystal. Black circles are experimental data (I_{obs}), and blue vertical lines show the position of Bragg's peaks. (c) Crystal structure image of $LaTe_3$, generated by VESTA software using lattice parameters as input.

plane due to bilayer splitting [13]. The dispersion is identical along the a and c axes but minimal along the b axis. The CDW instability opens up large gaps on the parts of Fermi surface showing most favorable propensity for nesting [12]. Notwithstanding much work recently, tuning of CDW order via modification of fermiology under appropriate perturbations remains a largely unaddressed issue. Such an endeavor can help to illuminate the effect of a CDW-reconstructed Fermi surface on the transport properties, and ultimately to help constrain theoretical models for the CDW state itself. Furthermore, the possibility of modifying or unearthing quantum orders by inducing changes in the underlying electronic structure with an appropriate perturbation is an issue of considerable and broad general interest in quantum matter. $LaTe_3$ presents the opportunity to avoid the complications due to magnetism, and we address these issues through extensive magnetotransport experiments and density-functional theory (DFT) plus dynamical mean-field theory (DMFT) calculations in this nonmagnetic candidate material.

II. MATERIAL AND METHODS

A. Single-crystal growth

Single crystals of $LaTe_3$ were grown via a tellurium flux technique, similar to a previous report [12]. At first, high-purity La (Alfa Aesar 99.9%) and Te (Alfa Aesar 99.99%) were taken in an alumina crucible with a molar ratio of $La_{0.025}Te_{0.975}$. Next, the crucible was sealed in a quartz tube under vacuum (10^{-5} Torr). The tube was put in a box furnace vertically and heated to 900 °C at 60 °C/h. It was then kept for 12 h and slowly cooled over a period of 4 days to end temperature 600 °C. Finally, we separated the excess tellurium by a high-temperature centrifuge. The flux-grown single crystals of $LaTe_3$ are platelike in shape and gold colored. The crystals were freshly cleaved before characterizations and measurements. Phase purity and the structural analysis of the samples were performed using the high-resolution x-ray diffraction (XRD) in Rigaku, TTRAX III, using Cu $K\alpha$ radiation. The resistivity measurements of $LaTe_3$ single crystals were performed using the standard four-probe technique. Electrical contacts were made using conductive silver paste and thin gold wire. The transport measurements were carried out in a 9 T physical property measurement system (Quantum Design). At first, the freshly cleaved single crystal of vdW-layered material $LaTe_3$ was cut into rectangular bar shapes. Then we placed voltage and current terminals across the sample and applied the silver paint in such a way that it ensures the homogeneous distribution of current density both across width (w) and thickness (t) directions. The schematic of the electrical contact configuration has been shown in Fig. 1(a). We have performed several independent magnetotransport measurements on same and different single crystals, and the results are reproducible within experimental error.

B. Details of first-principles and transport calculations

We combine DFT and DMFT in order to examine the electronic structure and resulting properties of $LaTe_3$. Calculations are based on the experimentally determined *Cmcm* structure and lattice parameters, as described in the present and earlier studies [12,13]. DFT calculations for $LaTe_3$ have been performed using the WIEN2K full-potential linearized augmented plane wave *ab initio* package [20,21]. For the calculations, 1000 k-points ($10 \times 10 \times 10$ mesh), cutoff parameter $Rk_{max} = 7.5$ (R is the smallest muffin-tin radius and k_{max} is the cutoff wave vector of the plane-wave basis set), and the generalized gradient approximation Perdew-Burke-Ernzerhof exchange-correlation potential were chosen. The muffin-tin radius (R) (a.u.) was set to 2.5. These parameters are converged such that energy convergences are accurate to 0.0001 eV in the irreducible Brillouin zone. Calculations are carried out in both without and with a magnetic field with inclusion of spin-orbit coupling (SOC). To include the effect of local correlations DMFT + iterated perturbation theory (IPT) calculations were carried out with input band structure from WIEN2K. The energy range for the calculations were taken from −10 to 10 eV to capture the higher-energy contribution of the Te5p orbitals to the density of states arising from the hybridization between p_x and p_z orbitals. Te p_x and p_z

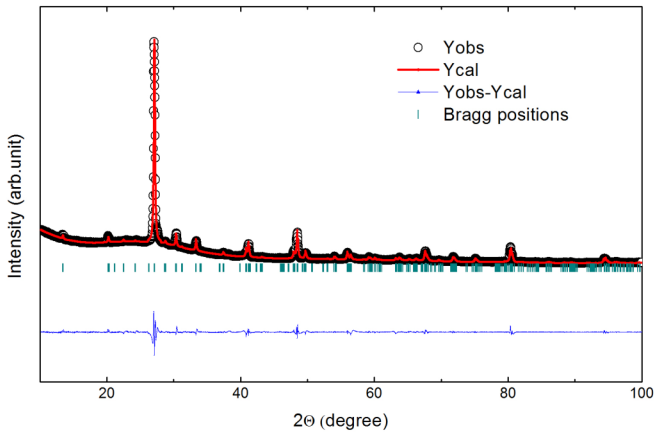

FIG. 2. Powder x-ray diffraction on crashed single crystals. The black open circles are experimental data (Y_{obs}), the red line is the calculated pattern (Y_{cal}), the blue line is the difference between experimental and calculated intensities (Y_{obs}-Y_{cal}), and the green lines show the Bragg positions.

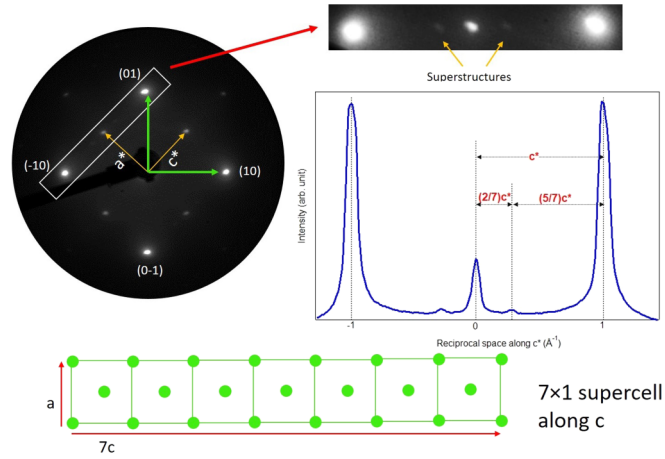

FIG. 3. Low-energy electron-diffraction image of the $LaTe_3$ single crystal at room temperature. The left panel shows low-energy electron-diffraction pattern. The top-right figure is the zoomed-in image of the diffraction spots. Two faint spots on both sides of the central spot represent superlattice structure. The superlattice periodicity in reciprocal space is $Q = 2/7c*$, which is elaborated in the bottom-left panel. This superlattice periodicity is associated with the high-temperature CDW state in $LaTe_3$ with the CDW transition temperature (T_{CDW}) presumed to be higher than 400 K. The figure at the bottom is the schematic of the supercell structure along the c axis.

orbitals, therefore, constitute a 2×2 Hamiltonian, which effectively results into two bands. The DMFT impurity problem was solved using the iterated perturbation theory approach. The multiorbital (MO) MO-IPT is used as an impurity solver in DMFT: Although not exact, it is a computationally fast and effective solver and has been proven to work very well in real multiband systems throughout all temperature range [22–24]. Correlation is induced via DMFT, which changes the noninteracting electronic structure significantly. Using the multiorbital DMFT (IPT) approach we have calculated the transport properties. To check the angular dependence of MR we have applied magnetic field in different directions from the b to the a axis which can be easily performed within the WIEN2K code. Two-dimensional cuts through the FS were extracted from WIEN2K on $200 \times 200\,k$-point grids for the local density approximation calculations.

C. Sample characterizations

X-ray diffraction was performed on the single-crystal sample. As shown in Fig. 1(b), the presence of very sharp (0 k 0) peaks in the diffraction pattern confirms that the flat plane of the crystal is perpendicular to the crystallographic b axis. Figure 2 shows the high-resolution x-ray diffraction pattern of the powdered sample of $LaTe_3$ crystals at room temperature. Within the resolution of XRD, we did not see any peak due to the impurity phase. Using the Rietveld profile refinement, all the peaks in the diffraction pattern can be indexed with an orthorhombic unit cell (space-group *Cmcm*) having $a = 4.392(2)$, $b = 26.245(6)$, and $c = 4.417(3)$ Å. The obtained values of lattice parameters are consistent with earlier reports [3,12,13]. Low-energy electron diffraction has been performed on a single crystal of $LaTe_3$ at 300 K, which has been illustrated and explained in Fig. 3. Two faint spots on both sides of the central diffraction spot as shown in the top right of Fig. 3 clearly indicates superlattice periodicity associated with the high-temperature CDW state (T_{CDW} presumed to be higher than 400 K) in $LaTe_3$.

III. EXPERIMENTAL RESULTS

A. Resistivity and transverse magnetoresistance

The zero-field resistivity (ρ_{xx}) is metallic over the whole temperature range as shown in Fig. 4(a). ρ_{xx} shows strong linear-in-T dependence at high temperatures followed by a smooth crossover to $\rho_{xx}(T) \simeq \rho_0 + AT^2$ at low temperatures as evident from the ρ_{xx} vs T^2 plot in the inset of Fig. 4(a). The coefficient A ($= 1.8 \times 10^{-6}\ \mu\Omega\,\mathrm{m/K^2}$) is found to be small. This suggests that the electronic correlation in $LaTe_3$ is weak. The small value of ρ_{xx} at 2 K ($\sim$0.45 $\mu\Omega$ cm) and the large residual resistivity ratio (RRR), $\rho_{xx}(300\ \mathrm{K})/\rho_{xx}(2\ \mathrm{K}) \sim 270$, testify the high quality of the $LaTe_3$ crystal. Similar metallic behavior of ρ_{xx} has also been reported with a RRR ($\sim$120) [8,13]. The reason behind the metallic behavior of ρ_{xx} below T_{CDW} is the partial gap opening in the multisheeted Fermi surface due to imperfect nesting. The temperature dependence of ρ_{xx} becomes more exciting under the application of the magnetic field in $B \parallel b$ and $I \parallel c$ configuration, which has been shown in Fig. 4(b). A humplike feature gradually develops which shifts toward higher temperature with increasing field strength. The derivative of $\rho_{xx}(T)$ in Fig. 4(c) clearly demonstrates that the position and sharpness of the anomaly depend strongly on the strength of the magnetic field. In several magnetic $R\mathrm{Te_3}$ compounds, similar humplike features in $\rho_{xx}(T)$ have been observed in the absence of external magnetic fields, which have been established as a characteristic signature of second CDW transition [10,11,16,17]. Figure 5(a) shows the field dependence of the transverse magnetoresistance (TMR) on the same $B \parallel b$ and $I \parallel c$ configurations where MR is defined as $\frac{[\rho_{xx}(B)-\rho_{xx}(0)]}{\rho_{xx}(0)} \times 100\%$. At 2 K and 9 T, the value of TMR is as large as $\sim$700%, and it diminishes rapidly with

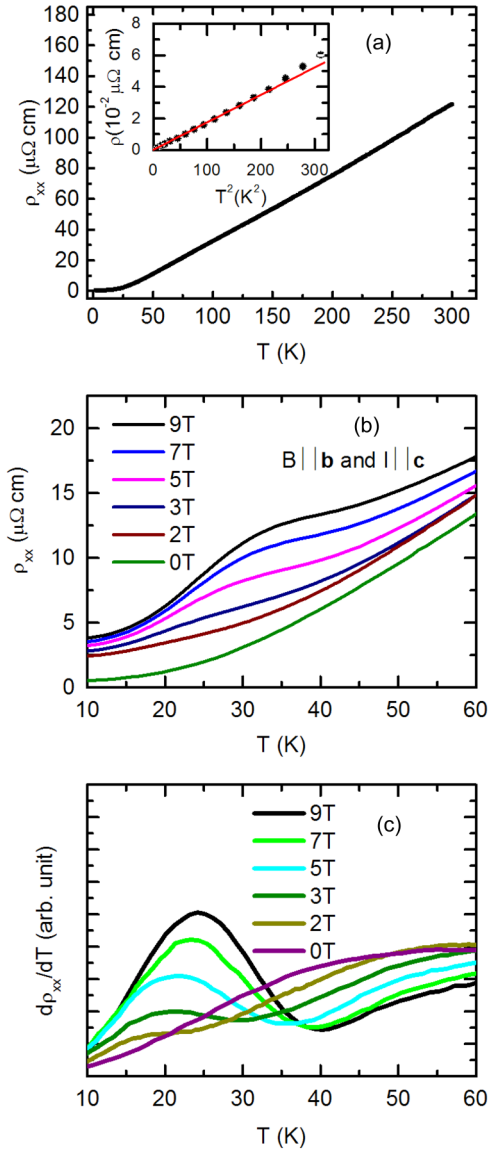

FIG. 4. Temperature dependence of resistivity. (a) Temperature dependence of resistivity (ρ_{xx}) from 2 to 300 K in the absence of magnetic-field (B). The inset shows $\rho_{xx}(T)$-ρ_0 at low temperatures, plotted as a function of T^2. The red solid line is the linear fit to the experimental data. The temperature dependence of ρ_{xx} starts to deviate from T^2 behavior above ∼15 K and smoothly crosses over to linear in T dependence above 20 K. (b) $\rho_{xx}(T)$ up to 60 K at different external magnetic-field strengths. (c) The first-order derivative of $\rho_{xx}(T)$ to clearly locate the position of the hump in $\rho_{xx}(T)$.

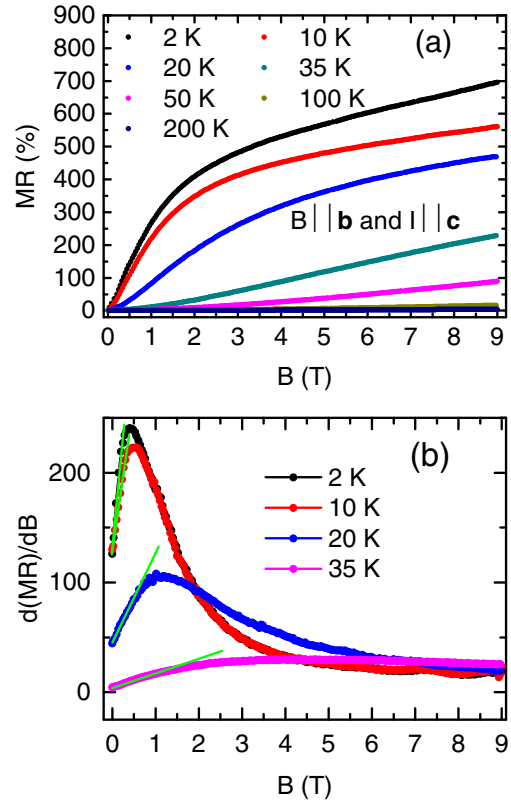

FIG. 5. Magnetic-field dependence of resistivity in transverse configuration. (a) TMR as a function of B at some representative temperatures in $B \parallel b$ and $I \parallel c$ configurations. (b) First-order derivative of MR as a function of B at representative temperatures 2, 10, 20, and 35 K. The green straight line is a guide to eye, showing the linear-in-B region of $\frac{d(MR)}{dB}$.

increasing temperature. Interestingly, TMR increases monotonically with increasing B without any sign of saturation up to 9 T. TMR exhibits two distinct regimes: a low-field quadratic B dependence and a high-field linear B dependence, connected by a smooth crossover. With increasing T, the crossover shifts towards higher B. The crossover in TMR is more clearly visible in the $\frac{d(\mathrm{TMR})}{dB}$ vs B plot as shown in Fig. 5(b). Although the $\frac{d(\mathrm{MR})}{dB}$ is linear in B at the low field, indicated by the green solid lines, it saturates at the high field. With increasing temperature, the low-field quadratic region in MR(B) increases, and as a consequence, the crossover from quadratic to linear MR shifts to the higher field. A nonsaturating MR along with the linear-in-B dependence is very interesting. This observation raises the enticing question about the nature of the hitherto uninvestigated electronic state of $LaTe_3$ at the high magnetic field.

Armed with the knowledge that the Fermi surface of $LaTe_3$ is diamond shaped on the ac plane with minimal b-axis dispersion, we have measured TMR by rotating the field from the b to the a axis within the ab plane. The schematic of the experimental setup is shown in Fig. 6(a). Figures 6(b)–6(d) show the angular variation of TMR at different fields at temperatures 2, 20, and 50 K, respectively. It is clear from these figures that TMR(θ) shows twofold rotational symmetry. At 2 K and 0.5 T, TMR exhibits a minimum for $B \parallel a$ ($\theta = 90°$) and a maximum for the $B \parallel b$ ($\theta = 0°$) direction and $\frac{\mathrm{TMR}(\theta=0)}{\mathrm{TMR}(\theta=90°)} \simeq 1.35$. With increasing B, initially this ratio increases and reaches ∼2.3 at 1 T and then decreases monotonically to a value of ∼0.88 at 9 T [Fig. 6(e)]. Thus, the low-field anisotropy in TMR reverses at high fields, a very unexpected characteristic that should ultimately have links to drastic modification of the electronic structure with B. One can argue from the figures that only the cos(θ)-like dependence in TMR, which has been observed at 2 K and low fields, survives for all the field strengths (up to 9 T) at high temperatures above 20 K. The polar plots of TMR for different applied fields are

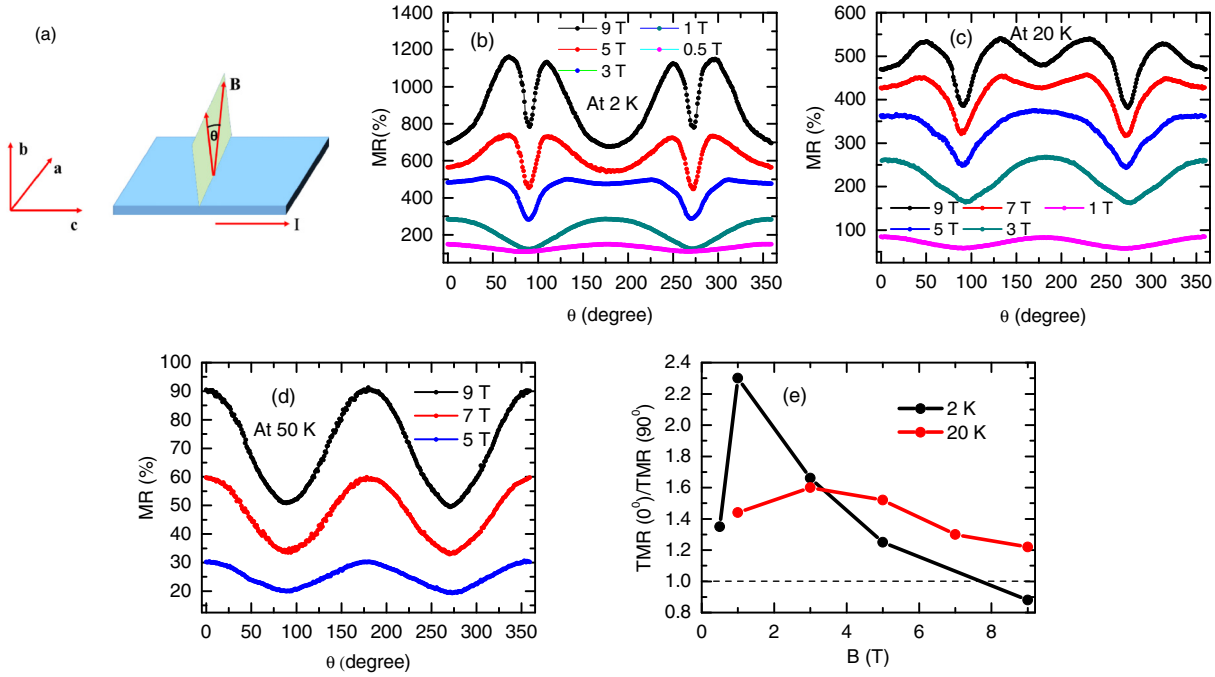

FIG. 6. Crystallographic direction dependence of TMR. (a) A schematic of the experimental configuration. The direction of the magnetic field has been varied from the b to the a axis, making an angle θ. (b)–(d) are the θ dependence of TMR for different constant magnetic-field strengths at 2, 20, and 50 K, respectively. (e) The field dependence of TMR(0°)/TMR(90°) at 2 and 20 K.

shown in Fig. 12 of the Appendix. It is rewarding to make an analogy between the B dependence of TMR in Fig. 5(a) and the TMR(θ) at different field strengths in Figs. 6(b)–6(d) at a particular temperature. In the low-field region where the TMR is quadratic in B, TMR(θ) shows cosinelike angular variation. On the other hand, at high fields where TMR is linear in B, TMR(θ) exhibits sinelike dependence. This reveals strong causal connections between the quadratic-in-B MR and the cosinelike TMR(θ), and between the linear MR and the sinelike TMR(θ). Thus, a tantalizing question arises: Is there a field-induced Fermi-surface reconstruction with the high-B state exhibiting anomalies famously associated with semimetallic behavior?

B. Longitudinal magnetoresistance

Temperature dependence of resistivity under application of magnetic field has also been measured in the longitudinal setup with the $B \parallel I \parallel c$ configuration and shown in Fig. 7(a). At 9 T, the humplike feature can be observed in $\rho_{xx}(T)$ at around 28 K. Although the anomaly is weaker compared to that observed in Fig. 4(b) (transverse case), it is clearly visible in the $\frac{d\rho}{dT}$ vs T plot in the inset of Fig. 7(a). Also, the hump appears at slightly lower temperature compared to that observed in transverse configuration. The much sharper increase in ρ with B for the longitudinal configuration weakens the anomaly and shifts its position toward lower temperature. As shown in Fig. 7(b) at 2 K and 9 T, the LMR is $\sim 10^3\%$. The LMR sharply rises with increasing B, undergoes a crossover from an approximate linear over a narrow range of field to sublinear B dependence at high fields and remains nonsaturating up to 9 T. Our theoretical calculations, to be discussed in the latter section, also support the appearance of a hump in the $\rho_{xx}(T)$ curve for both transverse and longitudinal configurations. Figures 7(d)–7(f) show the angle dependence of MR at some representative field strengths for the experimental configuration shown in Fig. 7(c) and at temperatures 2, 20, and 50 K, respectively. The direction of the magnetic field has been varied from the b to the c axis, making an angle $(90^\circ\text{-}\phi)$ with the current direction, on the bc plane. We uncover a peculiar ϕ and B dependence of MR. As shown in Fig. 7(d) at 9 T and 2 K, the maximum value of MR occurs for $\phi = 90^\circ$ (LMR). MR(ϕ) shows that two weaker spikelike peaks appear symmetrically around the strongest peak at $\phi = 90^\circ$. The weakest (MR $\sim$ 590%) and intermediate (MR $\sim$ 770 %) peaks in MR are $\sim 17^\circ$ and $\sim 28^\circ$ away from the strongest one, respectively. With decreasing B, the height of the prominent peak at $\phi = 90^\circ$ reduces drastically, whereas the other peaks show higher immunity to the field. As a result, MR(ϕ) exhibits a minimum at $\phi = 90^\circ$ for $B < 3$ T. Figures 7(d)–7(f) show that the peak at $\phi = 90^\circ$ also becomes very weak with increasing T. At high temperatures, the nature of MR(ϕ) curve is to some extent similar to that observed at 2 K for low-field strengths.

C. Hall resistivity measurements and analysis

To determine the nature and density of the charge carriers, the Hall resistivity (ρ_{yx}) as a function of B has been measured in the temperature range of 2–300 K and shown in Fig. 8(a). At 300 K, ρ_{yx} is found to be negative and almost linear in B, indicating electron-dominated transport near room temperature. Upon reducing T, $\rho_{yx}(B)$ becomes nonlinear and changes sign at high fields. This implies the presence of both the electron- and the hole-type charge carriers, and their contributions to electronic transport are comparable to each other.

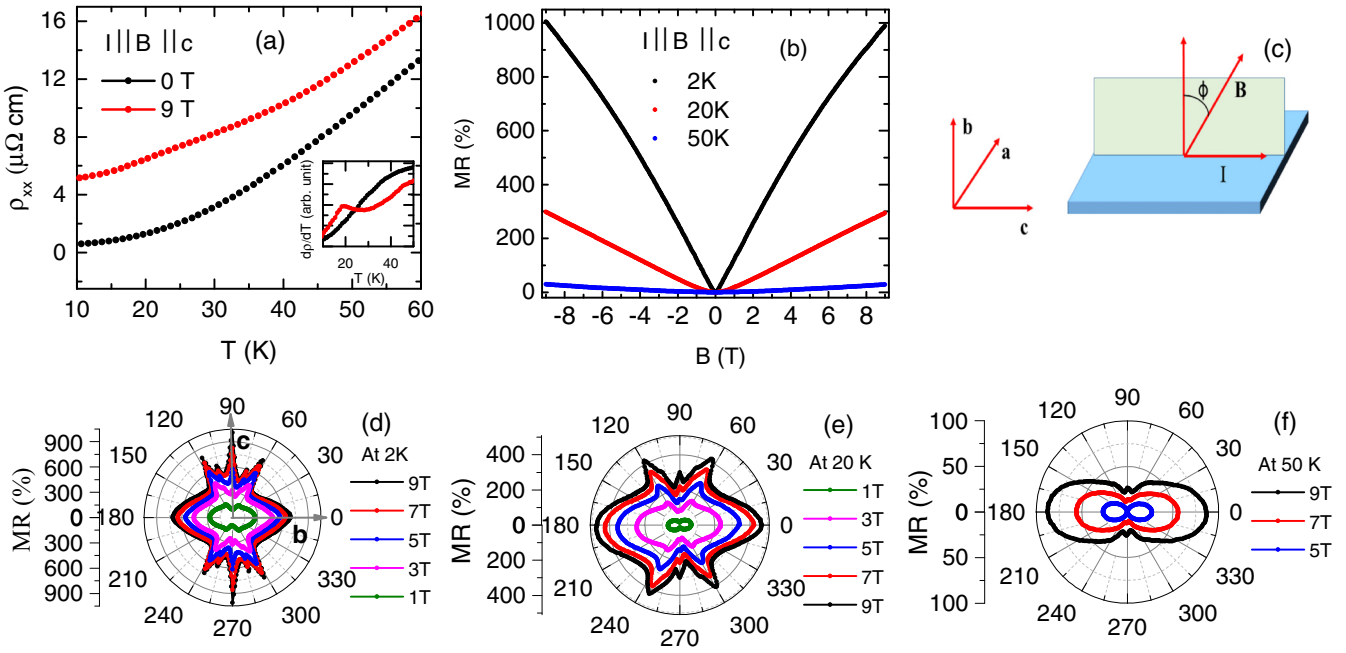

FIG. 7. Temperature and field dependences of magnetoresistance with $B \parallel I \parallel c$, and the angle between I and B is varied on the bc plane of the crystal. (a) Temperature dependence of resistivity (ρ_{xx}) at 0 and 9 T magnetic-field (B). The inset shows the first-order derivative of $\rho_{xx}(T)$ to clearly locate the position of the hump in $\rho_{xx}(T)$ under the application of the magnetic field. (b) Magnetic-field dependence of LMR at some representative temperatures. (c) Schematic illustrating the experimental configuration to measure the angular variation of MR on the bc plane. The direction of the magnetic field has been varied from the b to the c axis, making an angle (90°-ϕ) with the current direction. The polar plot of MR(ϕ) (d) at 2 K, (e) at 20 K, and (f) at 50 K, respectively, for some representative magnetic-field strengths.

We have performed simultaneous fitting (i.e., global fitting) of Hall conductivity ($\sigma_{xy} = \frac{\rho_{yx}}{\rho_{yx}^2+\rho_{xx}^2}$) and electrical conductivity ($\sigma_{xx} = \frac{\rho_{xx}}{\rho_{yx}^2+\rho_{xx}^2}$) data with the expressions derived from the semiclassical two-band model [25]. Figure 8(b) shows the theoretical fit to σ_{xy} and σ_{xx} with the expressions,

$$\sigma_{xy}(B) = \left[\frac{n_h\mu_h^2}{1+(\mu_h B)^2} - \frac{n_e\mu_e^2}{1+(\mu_e B)^2}\right]eB, \qquad (1)$$

and

$$\sigma_{xx}(B) = \left[\frac{en_h\mu_h}{1+(\mu_h B)^2} + \frac{\sigma_{xx}(0) - en_h\mu_h}{1+(\mu_e B)^2}\right]. \qquad (2)$$

n_e (n_h) and μ_e (μ_h) are electron (hole) density and electron (hole) mobility, respectively. The obtained values of n_e and n_h are $\sim 6.8 \times 10^{19}$ and 7.0×10^{20} cm^{-3}, respectively. On the other hand, μ_e ($\sim 3.3 \times 10^4$ cm^2 V^{-1} s^{-1} at 2 K) is found to be significantly higher than μ_h ($\sim 0.5 \times 10^4$ cm^2 V^{-1} s^{-1}). Such large values of carrier mobility have not been reported earlier in any rare-earth tritellurides and are rare in CDW and vdW compounds. Interestingly, the value of carrier mobility is comparable to that recently observed in topological semimetals [26–29]. The density of charge carriers has also been estimated from the band-structure theory calculation. These values, $n_e = 6.9 \times 10^{19}$ and $n_h = 7.2 \times 10^{20}$ cm^{-3} are close to that obtained from the two-band fitting of electrical and

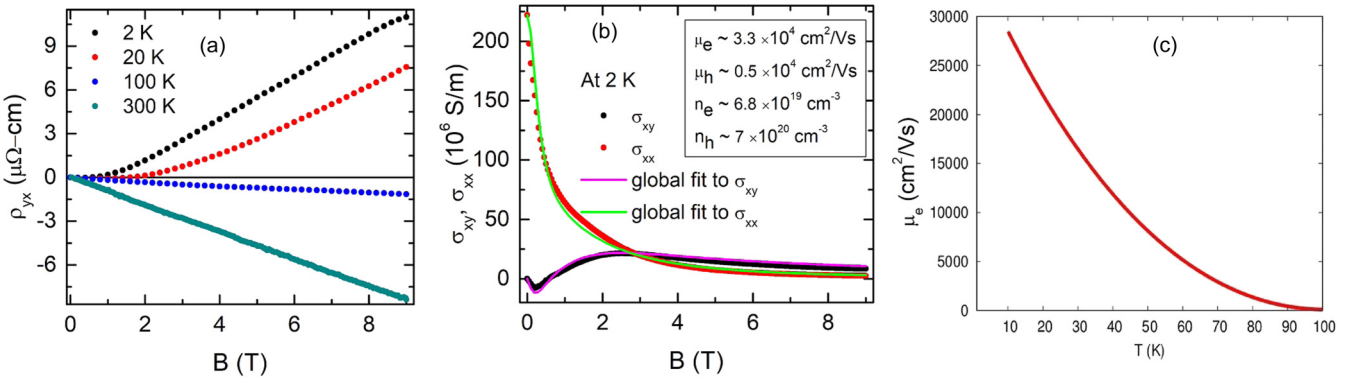

FIG. 8. Hall resistivity measurements and multiband analysis. (a) Field dependence of the Hall resistivity (ρ_{yx}) at different temperatures. (b) Global two-band fitting of the Hall conductivity ($\sigma_{xy} = \frac{\rho_{yx}}{\rho_{yx}^2+\rho_{xx}^2}$) and electrical conductivity ($\sigma_{xx} = \frac{\rho_{xx}}{\rho_{yx}^2+\rho_{xx}^2}$) at a representative temperature 2 K. (c) Theoretically estimated electron mobility from transport calculation and its temperature dependence.

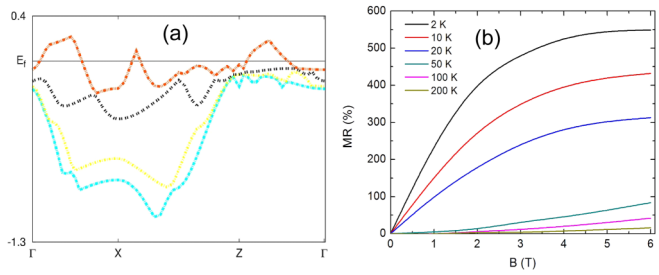

FIG. 9. Electronic band structure and field dependence of TMR from transport calculations. (a) Electronic band structure of $LaTe_3$ in the range of -1.3 to 0.4 eV about the Fermi level. The Fermi-level crossing band is from the Te p orbital. (b) TMR as a function of an external magnetic field up to 6 T at some representative temperatures and in the $I \parallel c$-axis and the $B \parallel b$-axis configurations.

Hall conductivities. Not only the carrier density, the electron mobility has also been estimated from transport calculations and shown in Fig. 8(c). The calculated mobility is close to that obtained from two-band fitting.

Transverse magnetoresistance in a nonmagnetic compound is typically orbital in nature, and it scales with the mobility (μ) of charge carriers on the plane perpendicular to the applied magnetic field [30,31]. So materials having high carrier mobility generally show large MR. Famously, compensation or near compensation of electrons and holes also results in large and nonsaturating transverse MR: Instances would be elemental bismuth [32] and possibly some recently discovered topological semimetals [26,33]. From the Hall measurements and analysis, band-structure theory, and transport calculations, it is evident that the mobility of charge carriers in $LaTe_3$ is very large and the contribution of electrons and holes to transport is comparable. This might be the possible explanation for the large and nonsaturating MR in $LaTe_3$.

IV. DISCUSSIONS BASED ON BAND-STRUCTURE, FERMI-SURFACE, AND TRANSPORT CALCULATIONS

We combine DFT and DMFT in order to examine the electronic structure and resulting properties of $LaTe_3$. Calculations are based on the experimentally determined *Cmcm* structure and lattice parameters, as described in the present and earlier studies [12,13]. From DFT + DMFT and transport (involving the full DFT + DMFT propagators without irreducible vertex corrections) calculations, we obtain the electronic band structure [Fig. 9(a)] as well as the field dependence of MR for the $I \parallel c$-axis and the $B \parallel b$-axis configurations [Fig. 9(b)]. Figure 9(a) shows that one band crosses the Fermi level and forms electronlike Fermi-surface sheets around the X point. In accord with previous work, the p band originating from planar Te atoms generates the Fermi surface [13]. Remarkably, the theoretically obtained field dependence of MR is very similar to that shown in Fig. 5(a) in all major respects. Moreover, the computed value of MR is also comparable to that observed in experiment. Several interesting features, germane to the magnetotransport findings, stand out from our DFT + DMFT studies and have been discussed in the following paragraphs.

(i) At zero field, the DFT Fermi surface [Fig. 10(a)] agrees with earlier band-structure calculations and ARPES measurements [12,13]. The FS in the parent state consists of inner and outer diamond sheets which are formed from the Te p_x and p_z orbitals. With zero magnetic-field the FS is symmetric along the k_x and k_z directions, but the symmetry is destroyed once the magnetic field is switched on. Furthermore, the Fermi surface for finite B [both in- and out-of-plane configurations as shown in Figs. 10(b) and 10(c), respectively] exhibits a reduction of in-plane curvature, suggesting gradual evolution toward more efficient nesting. This is very clear in Fig. 10(c), (in an in-plane field $B = 3.0$ T) where the reconstruction is particularly drastic: The Fermi surface now has large flat portions, almost perfectly nested with each other. Interestingly, the nesting tendency even between different Fermi sheets emerges at $B = 3.0$ T. Furthermore, since the inner closed Fermi-surface sheet arises predominantly from the Te p_x and p_z orbitals, the field-induced "flattening" of this sheet in an in-plane field $B = 3.0$ T actually suggests emergence of two quasi-one-dimensional (1D) bands, weakly hybridized with each other. Although this effect is weaker for out-of-plane fields, the reduction of in-plane Fermi-surface curvature is clearly visible in that case as well. Enhancement of flat regions in the Fermi surface immediately implies enhancement of scattering due to electron-electron and electron-phonon interactions, providing a direct insight into large and positive MRs.

(ii) Both electronic correlations and electron-lattice coupling renormalize the band dispersions and the DFT Fermi surface(s). Within local dynamical mean-field theory, a **k**-independent but energy (ω)-dependent self-energy generically

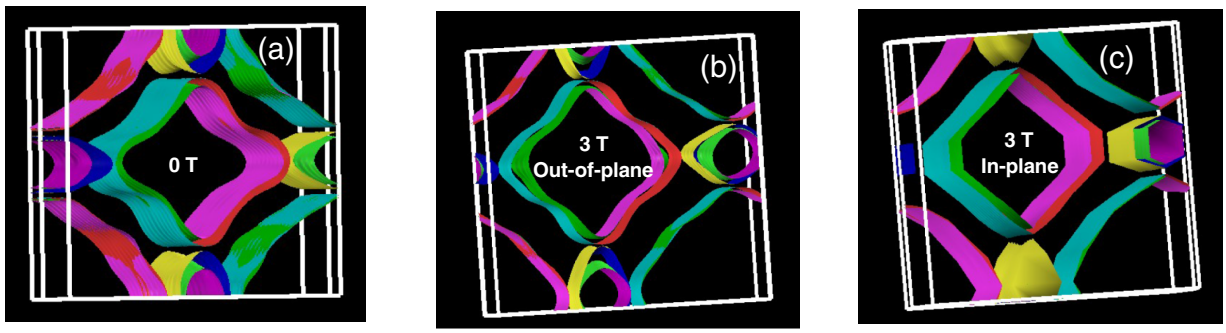

FIG. 10. Theoretically simulated Fermi surface in the presence and absence of an external magnetic field. Fermi surface of $LaTe_3$ (a) at zero field, (b) at 3 T out-of-plane, and (c) at 3 T in-plane magnetic field.

reduces the DFT band widths but leaves the shape and size of the Fermi surface nearly unaffected. However, in multiband systems, interactions can also lead to band-dependent renormalization of electronic states. We have carried out DFT + DMFT calculations by varying the intraorbital (U) and interorbital (U') interaction in the range of $0.0 < U \leqslant 2.0$ and $U' = 0.3U$. For $U = 1.0$ eV, self-energies for both p_x and p_z carriers exhibit a Landau-Fermi liquid form up to rather high T, i.e., $\mathrm{Im}\,\Sigma_{p_x,p_z}(\omega) \simeq -a\omega^2$ at low energy. Interestingly, for $U = 2.0$ eV, we uncover a coherence-incoherence (C-IC) crossover as a function of T: $\mathrm{Im}\,\Sigma_{p_x,p_z}(\omega) \simeq -a'\omega^2$ for $T < T_{\mathrm{coh}} \simeq 50$ K smoothly crosses over to $\simeq -A - a''\omega^2$ for $T > T_{\mathrm{coh}}$. Correspondingly, the dc resistivity crosses over from a quasilinear-in-T to a T^2 dependence at low temperatures, in nice qualitative accord with experiment. Even more interestingly, in a magnetic-field $B = 1$ T and for $U = 2.0$ eV, $\mathrm{Im}\,\Sigma_{p_z}(\omega)$ exhibits a (negative) polelike structure. This directly implies a rapid enhancement of the scattering rate in a magnetic field and can be rationalized in terms of a reduction of the DFT bandwidth (W) for $B > 0$, leading to stronger inelastic scattering and providing a possible explanation of positive MR. Remarkably, we find that the dc resistivity as well as the sign and magnitude of the MR agree quite well with experimental data, providing good support to this interpretation. It is interesting to note that the magnetic field-induced humplike feature in the $\rho(T)$ curve appears close to the coherence-incoherence transition temperature. The value of coefficient A has also been calculated theoretically which is about $1.2 \times 10^{-6}\ \mu\Omega\,\mathrm{m\,K^{-2}}$, close to the experimental value of A.

(iii) The emergence of a renormalized electronic structure comprising two "crossed" quasi-one-dimensional bands is quite interesting. Even a slight interaction on the carriers in two 1D, p_x and p_z derived, bands may have strong effects. It is interesting that intermediate-energy power-law frequency dependence of the optical conductivity in $R\mathrm{Te}_3$ systems has been observed [14], although the electronic origin of quasi-1D bands necessary for this picture has hitherto remained unclear here. An interchain $p_x - p_z$ hybridization favors Landau-Fermi-liquid coherence, and the interband electron-electron (electron-phonon) interactions, in turn, could be susceptible to instability to an unusual CDW state.

(iv) Our theoretical approach also gives very good agreement with details of both longitudinal and transverse MR as functions of in-plane and out-of-plane magnetic fields. The good accord with the T-dependent resistivity as well as the sign, magnitude, and nonsaturating nature of MR at the high field (at least, up to 9 T), permits a consistent interpretation of B, T, and angle-dependent MR in terms of a field-dependent Fermi-surface reconstruction (a field-induced Lifshitz transition) inside the CDW phase. We are unaware of such behavior *viz.*, a field-induced Lifshitz transition and the coherence-incoherence crossover in resistivity occurring well below T_{CDW} in transition-metal and rare-earth trichalcogenides.

In nonmagnetic materials, the LMR is usually found to be negligible. Although one could conceive of several alternative scenarios, they fall short of providing a unified rationalization of the above observations. A more plausible scenario could be the following. In a few ultraclean metals, the LMR can be large and positive and tends to saturate at high fields [34,35]. It has been ascribed to the multiply connected nature of the Fermi surface through Brillouin-zone boundaries. When the cross-sectional area of the Fermi surface is large in the neck regions, the conductivity experiences strong suppression in an external magnetic field. The calculated Fermi surfaces, shown in Figs. 10(a)–10(c) and in Figs. 13(a)–13(c) in the Appendix, are indeed multiply connected across the Brillouin-zone boundaries. Although one could ascribe large and positive LMR to this aspect, the lack of saturation up to 9 T magnetic field fall short to explain the above behavior of the LMR.

The sizable field-induced FS reconstruction we find affords an explanation of the TMR data. We notice that similarities between the observed TMR of LaTe_3 and those of other materials with spin- and charge-density-wave states [36] suggest that the crossover from $\Delta\rho \sim B^2$ to $\Delta\rho \sim |B|$ with increasing B may be intrinsic to field-driven changes in FS as follows: The FS undergoes a clear "topological" change from a smoothly curved at small B to: (i) pockets with very flat parallel sheets, and more importantly, to (ii) several small pockets with sharp corners. Carrier motion around these sharp corners of FS will dominate the MR (over contributions from flat parts of the FS) because large enhancement of the cyclotron frequency ω_c at the corners will sizably enhance $\omega_c\tau$ [37]. Pippard showed that a square FS with infinitely sharp corners gives $\Delta\rho \sim |B|$, a behavior persisting as long as the mean free path l_k of the charge carrier is much larger than r_k, the cyclotron radius at the sharp corner [37]. A perusal of theoretically simulated FS clearly shows that the large linear MR is intimately correlated with the emergence of such a field-reconstructed Fermi surface.

Thus, the crossover from B^2 to a $|B|$ variation of the MR is intricately tied to the drastic modification of FS topology in modest magnetic fields. Within our modeling, this can be understood as a manifestation of the interplay between the $\mathbf{k}$-dependent interband hybridization [$V(\mathbf{k})$] and the SOC (λ). Although the former is of the order of 200 meV, sizably larger than the latter, about 20 meV at the bare level, even small local Coulomb interactions could change this picture: V is renormalized downward to $V_{\mathrm{ren}}(\mathbf{k}) = z_p,\ V(\mathbf{k}) \simeq 50$ meV, ($z_p \simeq 0.25$ is the quasiparticle weight of the p -band) and the SOC, being a local quantity, is expected to be mildly enhanced by local correlations. Thus, when $\lambda/V_{\mathrm{ren}}(\mathbf{k})$ is not small (about 0.4), the considerable k-space rearrangement of electronic states occurs due to interplay between the Zeeman energy ($g\mu_B B$), λ, and $V_{\mathrm{ren}}(\mathbf{k})$: The coherent interband hybridization is sizably suppressed as a result, directly leading to destruction of FS warping features and the emergence of flat parallel portions with sharp edges in Figs. 10(b) and 10(c). This is the underlying mechanism for the striking sensitivity of the FS to a modest magnetic field we find in DFT + DMFT.

Moreover, the anomalous behavior of MR(ϕ) wherein spikelike peaks at the intermediate angles appear when the direction of magnetic field is changed from the $B \parallel b$ to the $B \parallel c \parallel I$ configuration, testifies to a geometrical effect due to the quasi-two-dimensional nature of the Fermi surface(s) [34,38–40]. In high-purity layered metallic systems, at some characteristic angles, known as Yamaji angles, the cyclotron orbits on the corrugated Fermi surface acquire equal cross-sectional

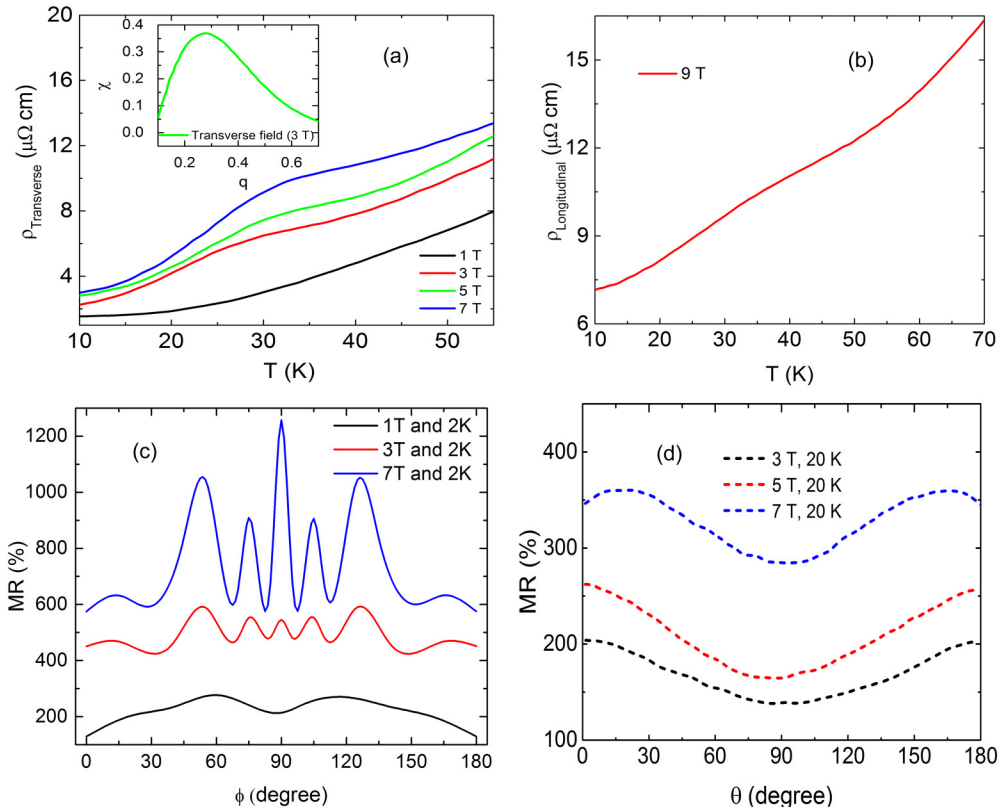

FIG. 11. Calculated transport properties and theoretically obtained susceptibility plots. Resistivity as a function of temperature both in the absence and the presence of B in the: (a) $I \parallel c$-axis and $B \parallel b$-axis configuration as in Fig. 4(b) and (b) the $B \parallel I \parallel c$-axis configuration as in Fig. 7(a). The susceptibility plot, obtained at representative field strength 3 T for the transverse field configuration has been shown in the inset of (a). The χ plot which has been obtained at 30 K indicates the possible low-temperature CDW with $Q = 1/3a*$. (c) MR as a function of angle between current and magnetic field on the bc plane of the crystal. (d) Crystallographic direction dependence of TMR which has been observed by rotating the direction of the magnetic field about current parallel to the c axis.

areas. As a consequence, the Landau orbits become nondispersive and the group velocity of electrons perpendicular to the layers vanishes, leading to a peak in the resistivity. In the present material, MR(ϕ) shows strong Yamaji peaks at $\sim 73^\circ$ and $\sim 62^\circ$. This clearly shows the significant contribution of the CDW-reconstructed Fermi surfaces to the geometrical effect in MR(ϕ). The suppression of Yamaji peaks with increasing temperature may result from: (i) thermal broadening of Landau orbital states in a pure one-electron band-structure view or (ii) in a correlated view, the C-IC crossover in $LaTe_3$ occurs at $T_{coh} \simeq 50$ K for $B = 0$, which results in a loss of the Landau quasiparticles themselves. Since the Fermi surfaces show marked propensity towards development of flatter sections for $B > 0$, one expects a reduction of the one-electron bandwidth and, hence, of the C-IC crossover scale with B, leading to damping out of the Fermi surfaces themselves above $T_{coh}(B)$.

As mentioned earlier, in the absence of a magnetic field, the magnetic rare-earth tritellurides exhibit a second CDW transition (T_{CDW2}) at a much lower temperature in a perpendicular direction to the higher-temperature one, around the wave-vector $Q = 1/3a*$. Temperature dependence of resistivity shows a weak anomaly at T_{CDW2}. The nonmagnetic tritellurides, however, do not show this low-temperature CDW transition [4,10–12,16,17]. In $LaTe_3$, the appearance of a humpike feature in the $\rho(T)$ curve with an applied field and the systematic enhancement of its sharpness with increasing field strength appear to suggest a connection of this anomaly to a field-induced CDW transition. To probe this connection, we have performed a charge-susceptibility calculation at 30 K in the presence of the 3 T external magnetic field. The susceptibility plot in the inset of Fig. 11(a) (at the transverse field configuration as representative), shows a peak at $Q = 1/3a*$. This suggests that the magnetic field is likely to induce an additional low-temperature CDW state in the nonmagnetic $LaTe_3$ at the same value of Q as observed in magnetic RTe_3 compounds in the absence of a magnetic field. Similar results have also been obtained for the longitudinal configuration in our susceptibility calculation. Considering the propensity of the field-reconstructed Fermi surface towards enhanced nesting, the low-temperature hump in resistivity-temperature curves [Figs. 4(b), 4(c) and 7(a)] has been successfully reproduced from theoretical calculations and shown in Figs. 11(a) and 11(b) for the transverse and longitudinal configurations, respectively. The position of the hump, its variation with field strength, and its intensity over background resistivity are in good agreement with experimental findings.

The theoretically computed MR(ϕ) [Fig. 11(c)] shows fairly good agreement with experimental results [Fig. 7(d)]. Both the number of MR peaks and their positions are

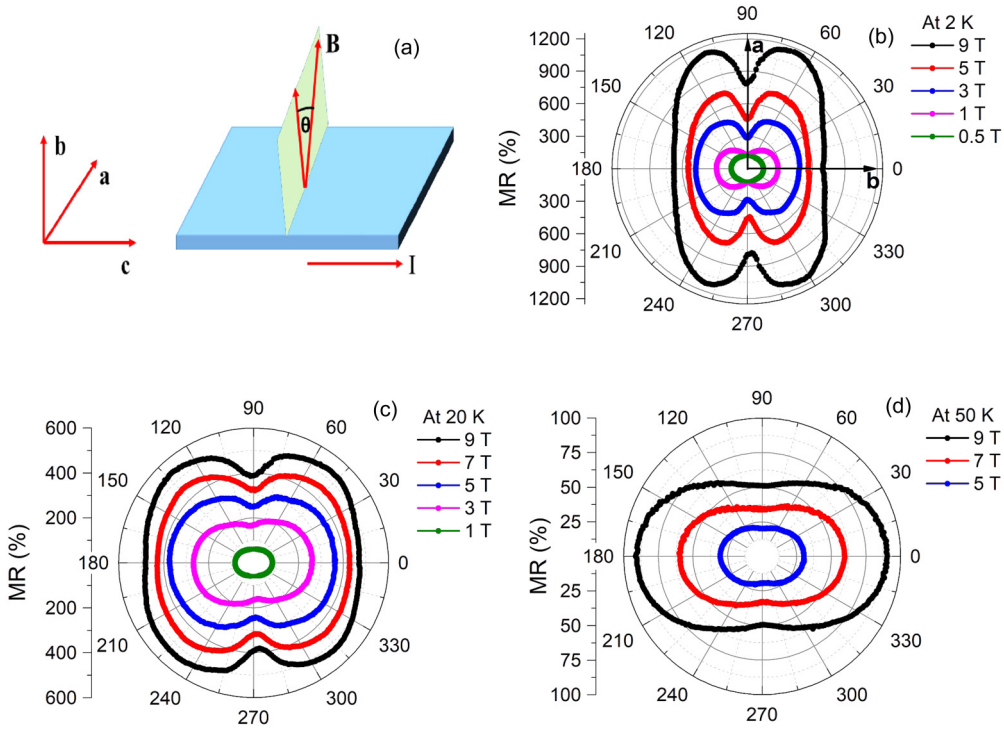

FIG. 12. Polar plot of TMR (θ). (a) The experimental configuration for the angular variation of TMR. (b)–(d) are the polar plots of TMR (θ) at 2, 20, and 50 K, respectively.

successfully reproduced by theory. Furthermore, the magnitudes of the MR in both cases at a given angle are also comparable to experimental values of MR. Similar to MR(ϕ), the experimental MR(θ) as shown in Fig. 6(c) is also well reproduced in transport calculations [Fig. 11(d)]. Not only the angle dependence and the value of MR, but also the extreme sensitivity of the angular variation of MR(ϕ) and MR(θ) on the field is reproduced by theory as evident in Figs. 11(c) and 11(d). This testifies to the intimate link of these features with the field-induced modification of the Fermi surface as shown in Figs. 10(a)–10(c). Taken together, these findings support a field-induced Lifshitz transition of the zero-field FS.

V. CONCLUSION

In conclusion, the present research demonstrates a hitherto uninvestigated through electronic transport experiments on a candidate of rare-earth tritellurides $LaTe_3$. We observe several intriguing phenomena in the magnetotransport properties, rarely seen in any CDW system. Manifestations of the interplay between CDW order and field-induced electronic structure modification in a nonmagnetic material has been exposed. The study holds promising potential to establish route to tune CDW states. In addition, Hall measurements supported by our transport calculation reveals an unexpected high mobility of charge carriers, which has remained elusive for these CDW and vdW materials. The unique coexistence of weak interlayer van der Waals coupling, CDW state, interplay of CDW with external perturbation like magnetic field, and the huge mobility of charge carriers, may have a promising impact on technological applications and device fabrication.

ACKNOWLEDGMENTS

We acknowledge Prof. S. Roy Barman and his group the UGC-DAE Consortium for Scientific Research, Indore for low-energy electron diffraction measurements. S.K. acknowledges the support from DST Women Scientist Grant No. SR/WOS-A/PM-80/2016(G).

APPENDIX

1. Polar plot for TMR(θ)

The angle dependence of transverse magnetoresistance, which has been discussed in the main text [Figs. 6(b) and 6(c)], is also represented in a polar plot and shown in Fig. 12.

2. Theoretically simulated Fermi surface under 1 T magnetic field

In Figs. 13(b) and 13(c), we have shown the Fermi surface at 1 T both in-plane and out-of-plane configurations of a magnetic field.

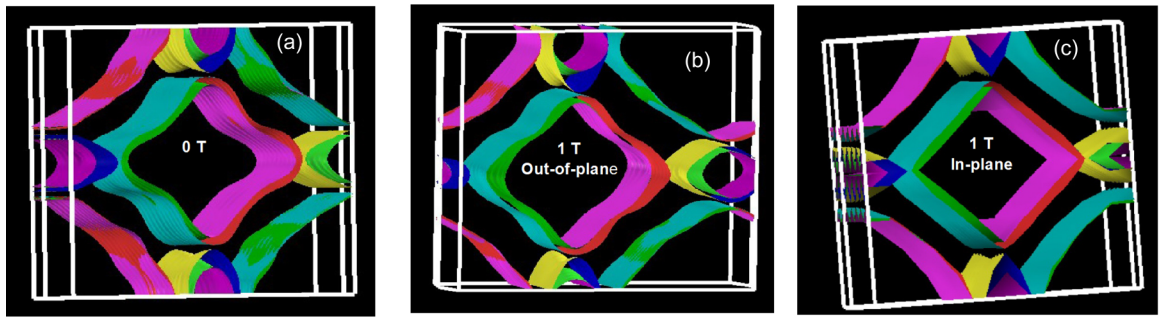

FIG. 13. Reconstruction of the Fermi surface under 1 T out-of-plane and 1 T in-plane magnetic field. Fermi surface (a) at zero field, (b) at 1 T out-of-plane, and (c) at 1 T in-plane external magnetic fields.

[1] S. Manzeli, D. Ovchinnikov, D. Pasquier, O. V. Yazyev, and A. Kis, 2D transition metal dichalcogenides, Nat. Rev. Mater. **2**, 17033 (2017).

[2] T. H. Ramsey, H. Steinfink, and E. J. Weiss, The phase equilibria and crystal chemistry of the rare earth-group VI systems. IV. lanthanum-tellurium, Inorg. Chem. **4**, 1154 (1965).

[3] B. K. Norlinga and H. Steinfink, The crystal structure of neodymium tritelluride, Inorg. Chem. **5**, 1488 (1966).

[4] E. DiMasi, M. C. Aronson, J. F. Mansfield, B. Foran, and S. Lee, Chemical pressure and charge-density waves in rare-earth tritellurides, Phys. Rev. B **52**, 14516 (1995).

[5] V. Brouet, W. L. Yang, X. J. Zhou, Z. Hussain, N. Ru, K. Y. Shin, I. R. Fisher, and Z. X. Shen, Fermi Surface Reconstruction in the CDW State of $CeTe_3$ Observed by Photoemission, Phys. Rev. Lett. **93**, 126405 (2004).

[6] J. Laverock, S. B. Dugdale, Z. Major, M. A. Alam, N. Ru, I. R. Fisher, G. Santi, and E. Bruno, Fermi surface nesting and charge-density wave formation in rare-earth tritellurides, Phys. Rev. B **71**, 085114 (2005).

[7] K. Yumigeta, Y. Qin, H. Li, M. Blei, Y. Attarde, C. Kopas and S. Tongay, Advances in rare-earth tritelluride quantum materials: Structure, properties, and synthesis, Adv. Sci. **8**, 2004762 (2021).

[8] N. Ru and I. R. Fisher, Thermodynamic and transport properties of YTe_3, $LaTe_3$, and $CeTe_3$, Phys. Rev. B **73**, 033101 (2006).

[9] H. Chudo, C. Michioka, Y. Itoh, and K. Yoshimura, Te^{125} and La^{139} NMR studies of single crystal $LaTe_3$, J. Phys. Soc. Jpn. **76**, 123708 (2007).

[10] N. Ru, C. L. Condron, G. Y. Margulis, K. Y. Shin, J. Laverock, S. B. Dugdale, M. F. Toney, and I. R. Fisher, Effect of chemical pressure on the charge density wave transition in rare-earth tritellurides RTe_3, Phys. Rev. B **77**, 035114 (2008).

[11] N. Ru, J.-H. Chu, and I. R. Fisher, Magnetic properties of the charge density wave compounds RTe_3 (R = Y, La, Ce, Pr, Nd, Sm, Gd, Tb, Dy, Ho, Er, and Tm), Phys. Rev. B **78**, 012410 (2008).

[12] V. Brouet, W. L. Yang, X. J. Zhou, Z. Hussain, R. G. Moore, R. He, D. H. Lu, Z. X. Shen, J. Laverock, S. B. Dugdale, N. Ru, and I. R. Fisher, Angle-resolved photoemission study of the evolution of band structure and charge density wave properties in RTe_3 (R = Y, La, Ce, Sm, Gd, Tb, and Dy), Phys. Rev. B **77**, 235104 (2008).

[13] N. Ru, R. A. Borzi, A. Rost, A. P. Mackenzie, J. Laverock, S. B. Dugdale, and I. R. Fisher, de Haas-van Alphen oscillations in the charge density wave compound lanthanum tritelluride $LaTe_3$, Phys. Rev. B **78**, 045123 (2008).

[14] A. Sacchetti, C. L. Condron, S. N. Gvasaliya, F. Pfuner, M. Lavagnini, M. Baldini, M. F. Toney, M. Merlini, M. Hanfland, J. Mesot, J.-H. Chu, I. R. Fisher, P. Postorino, and L. Degiorgi, Pressure-induced quenching of the charge-density-wave state in rare-earth tritellurides observed by x-ray diffraction, Phys. Rev. B **79**, 201101(R) (2009).

[15] D. A. Zocco, J. J. Hamlin, T. A. Sayles, M. B. Maple, J.-H. Chu, and I. R. Fisher, High-pressure, transport, and thermodynamic properties of $CeTe_3$, Phys. Rev. B **79**, 134428 (2009).

[16] A. Banerjee, Y. Feng, D. M. Silevitch, J. Wang, J. C. Lang, H.-H. Kuo, I. R. Fisher, and T. F. Rosenbaum, Charge transfer and multiple density waves in the rare earth tellurides, Phys. Rev. B **87**, 155131 (2013).

[17] D. A. Zocco, J. J. Hamlin, K. Grube, J.-H. Chu, H.-H. Kuo, I. R. Fisher, and M. B. Maple, Pressure dependence of the charge-density-wave and superconducting states in $GdTe_3$, $TbTe_3$, and $DyTe_3$, Phys. Rev. B **91**, 205114 (2015).

[18] A. A. Sinchenko, P. D. Grigoriev, P. Lejay, and P. Monceau, Linear magnetoresistance in the charge density wave state of quasi-two-dimensional rare-earth tritellurides, Phys. Rev. B **96**, 245129 (2017).

[19] C. D. Malliakas and M. G. Kanatzidis, Divergence in the behavior of the charge density wave in $RETe_3$ (RE = rare-earth element) with temperature and RE element, J. Am. Chem. Soc. **128**, 12612 (2006).

[20] P. Blaha, K. Schwarz, G. K. H. Madsen, D. Kvasnicka, and J. Luitz, An Augmented Plane Wave + Local Orbitals Program for Calculating Crystal Properties (Karlheinz Schwarz, Technical Universität Wien, 2001).

[21] O. K. Andersen, Simple approach to the band-structure problem,, Solid State Commun. **13**, 133 (1973).

[22] S. Koley, M. S. Laad, N. S. Vidhyadhiraja, and A. Taraphder, Preformed excitons, orbital selectivity, and charge density wave order in $1T-TiSe_2$, Phys. Rev. B **90**, 115146 (2014).

[23] A. Taraphder, S. Koley, N. S. Vidhyadhiraja, and M. S. Laad, Preformed Excitonic Liquid Route to a Charge Density Wave in $2H$-$TaSe_2$, Phys. Rev. Lett **106**, 236405 (2011).

[24] S. Koley, N. Mohanta, and A. Taraphder, The unusual normal state and charge-density-wave order in $2H$-$NbSe_2$, J. Phys.: Condens. Matter **27**, 185601 (2015).

[25] C. M. Hurd, *The Hall Effect in Metals and Alloys* (Plenum, New York, 1972).

[26] C. Shekhar, A. K. Nayak, Y. Sun, M. Schmidt, M. Nicklas, I. Leermakers, U. Zeitler, Y. Skourski, J. Wosnitza, Z. Liu, Y. Chen, W. Schnelle, H. Borrmann, Y. Grin, C. Felser, and B. Yan, Extremely large magnetoresistance and ultrahigh mobility

in the topological Weyl semimetal NbP, Nat. Phys. **11**, 645 (2015).

[27] G. Zheng, X. Zhu, Y. Liu, J. Lu, W. Ning, H. Zhang, W. Gao, Y. Han, J. Yang, H. Du, K. Yang, Y. Zhang, and M. Tian, Field-induced topological phase transition from a three-dimensional Weyl semimetal to a two-dimensional massive Dirac metal in $ZrTe_5$, Phys. Rev. B **96**, 121401(R) (2017).

[28] L. P. He, X. C. Hong, J. K. Dong, J. Pan, Z. Zhang, and S. Y. Li, Quantum Transport Evidence for the Three-Dimensional Dirac Semimetal Phase in Cd_3As_2, Phys. Rev. Lett. **113**, 246402 (2014).

[29] R. Singha, A. K. Pariari, B. Satpati, and P. Mandal, Large non-saturating magnetoresistance and signature of nondegenerate Dirac nodes in ZrSiS, Proc. Natl. Acad. Sci. USA **114**, 2468 (2017).

[30] C. Jacoboni, *Theory of Electron Transport in Semiconductors* (Springer, Berlin, 2010).

[31] Z. Zhu, A. Collaudin, B. Fauqué, W. Kang, and K. Behnia, Field-induced polarization of dirac valleys in bismuth, Nat. Phys. **8**, 89 (2012).

[32] A. A. Abrikosov, Quantum linear magnetoresistance, Europhys. Lett. **49**, 789 (2000).

[33] M. N. Ali, J. Xiong, S. Flynn, J. Tao, Q. D. Gibson, L. M. Schoop, T. Liang, N. Haldolaarachchige, M. Hirschberger, N. P. Ong, and R. J. Cava, Large non-saturating magnetoresistance in WTe_2, Nature (London) **514**, 205 (2014).

[34] N. Kikugawa, P. Goswami, A. Kiswandhi, E. S. Choi, D. Graf, R. E. Baumbach, J. S. Brooks, K. Sugii, Y. Iida, M. Nishio, S. Uji, T. Terashima, P. M. C. Rourke, N. E. Hussey, H. Takatsu, S. Yonezawa, Y. Maeno, and L. Balicas, Interplanar coupling-dependent magnetoresistivity in high-purity layered metals, Nat. Commun. **7**, 10903 (2016).

[35] A. B. Pippard, Longitudinal magnetoresistance, Proc. R. Soc. London, Ser. A **282**, 464 (1964).

[36] Y. Feng, Y. Wang, D. M. Silevitch, J.-Q. Yan, R. Kobayashi, M. Hedo, T. Nakama, Y. Ōnuki, A. V. Suslov, B. Mihaila, P. B. Littlewood, and T. F. Rosenbaum, Linear magnetoresistance in the low-field limit in density-wave materials, Proc. Natl. Acad. Sci. USA **116**, 11201 (2019).

[37] A. B. Pippard, *Magnetoresistance in Metals* (Cambridge University Press, Cambridge, U.K., 1989).

[38] K. Yamaji, On the angle dependence of the magnetoresistance in quasi-two-dimensional organic superconductors, J. Phys. Soc. Jpn **58**, 1520 (1989).

[39] R. H. McKenzie and P. Moses, Incoherent Interlayer Transport and Angular-Dependent Magneto-Resistance Oscillations in Layered Metals, Phys. Rev. Lett. **81**, 4492 (1998).

[40] Y. J. Jo, J. Park, G. Lee, M. J. Eom, E. S. Choi, J. H. Shim, W. Kang, and J. S. Kim, Valley-Polarized Interlayer Conduction of Anisotropic Dirac Fermions in $SrMnBi_2$, Phys. Rev. Lett. **113**, 156602 (2014).